Accepted Article Preview: Published ahead of online publication

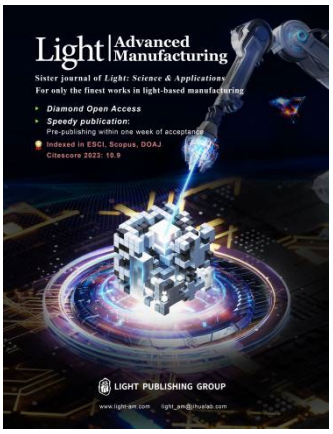

Plasmon excitation in graphene nanoribbon arrays on SiC

Anastasiia A. Kniazeva, Samvel R. Yegian, Sergey A. Dyakov, Andrey V. Muratov, Denis M. Zhigunov, Oleg A. Klimenko, Nikolay A. Gippius, and Vladimir N. Antonov

Cite this article as: Anastasiia A. Kniazeva, Samvel R. Yegian, Sergey A. Dyakov, Andrey V. Muratov, Denis M. Zhigunov, Oleg A. Klimenko, Nikolay A. Gippius, and Vladimir N. Antonov. Plasmon excitation in graphene nanoribbon arrays on SiC. *Light: Advanced Manufacturing* accepted article preview 24 June, 2026; doi: 10.37188/lam.2026.109

Received 7 January 2026; revised 19 June 2026; accepted 22 June 2026;
Accepted article preview online 24 June 2026

Kniazeva, et al. *Light*: *Advanced Manufacturing*
https://doi.org/10.1038/s41377-020-0333-9

Official journal of the JHL 2689-9620
http://www.light-am.com/

Plasmon excitation in graphene nanoribbon arrays on SiC

Anastasiia A. Kniazeva[1] †, Samvel R. Yegian[1], Sergey A. Dyakov[1], Andrey V. Muratov[2], Denis M. Zhigunov[1], Oleg A. Klimenko[1] [2], Nikolay A. Gippius[1], and Vladimir N. Antonov[1]

[1]*Skolkovo Institute of Science and Technology, Bolshoy Boulevard 30, bld. 1, Moscow, Russia*
[2]*PN Lebedev Physical Institute of RAS, Leninskiy prospekt 53, Moscow, Russia 119991*
*These authors contributed equally to this work.
†Correspondence to: Anastasiia Kniazeva: Anastasiya.Knyazeva@skoltech.ru

Abstract

Graphene-based structures have various prospective applications in optics and photonics. However, most of these applications require fabricating devices on an industrial scale. Currently, this can be achieved using two technologies: chemical vapour deposition (CVD) of graphene on a SiO_2 substrate (G-on-SiO_2), and epitaxial graphene formed on a SiC substrate (epi-G). In these technologies, graphene is strongly coupled to the substrate, causing it to affect the spatial distribution of the electromagnetic field and optical modes. In this study, we investigated plasmon excitation in the epi-G nanoribbon arrays. We showed that plasmon dispersion in epi-G nanoribbon arrays deviates from that predicted by the analytical model, which works well for G-on-SiO_2 structures. Simultaneosly, numerical simulations of epi-G plasmons using the Fourier modal method, which accounted for substrate-induced effects, appeared to agree well with the experimental spectra. We also demonstrated that epi-G structures provide a prospective platform for far- and mid-infrared photonic applications.

Keywords: Graphene, plasmon, graphene nanoribbon array, silicon carbide, Fourier-transform infrared spectroscopy, Fourier modal method.

Introduction

In recent years, the study of two-dimensional (2D) materials, such as graphene and other van der Waals structures, has attracted increased interest, because of the remarkable properties that render them highly suitable for optics and photonics [1, 2, 3, 4, 5, 6, 7]. The high local density of the optical states of confined plasmonic modes (larger by a factor of 10^6 than that in free space [8]) allows the development of surface-enhanced infrared absorption (SEIRA) spectroscopy. Similar to surface-enhanced Raman scattering [9, 10], SEIRA originates from resonant light–matter interactions and provides strong infrared (IR) field enhancement and confinement of incident light near the surface of a customised structure [11, 12]. Plasmon resonances in graphene nanoribbon (GNR) arrays—the leading mechanism of light–graphene interactions—have been studied in sufficient detail in chemical vapour deposition (CVD) of graphene samples on a SiO_2 substrate (G-on-SiO_2), where the technology allows the fabrication of large-scale patterns and can be implemented industrially [1, 11]. Depending on the ribbon width, the type of doping (i.e., electrical or chemical), and substrate material, the plasmon frequency in GNR arrays can be continuously tuned from the far-IR [13, 14] to the mid-IR frequency range [15, 8], fully covering the molecular fingerprint region (600 – 2000 cm^{-1}). The GNR arrays significantly enhance the IR absorption of organic molecules immobilised on graphene, thereby providing an effective platform for biosensing and chemical detection applications [16, 17]. Furthermore, gas molecules have been selectively identified by improved GNR-based sensors through the adsorptive redistribution of the molecules on graphene [18, 19]. In addition, SEIRA spectroscopy can be achieved by other resonant phenomena, such as the excitation of surface phonon polaritons (SPhPs) [20, 21] and hyperbolic phonon polaritons [12] appearing in the so-called reststrahlen bands (between the LO and TO phonon modes) [21], wherein plasmon modes are damped to enable spectral studies in a continuous spectrum from the far- to mid-IR range. In addition, graphene structures such as GNR arrays have been implemented as platforms for filters [22], selective polariser devices [23], sensors [18], and other devices [24, 25, 26].

An alternative to CVD graphene technology is the graphitisation of the Si-terminated face of silicon carbide

(SiC (001)) (epi-G), which has been less explored for large-scale applications [27, 28, 29]. Owing to its surface morphology [30, 31], epi-G demonstrates new effects that are hardly observable in CVD graphene devices: terahertz (THz) filtering by alternating ribbons of mono- and bilayer graphene [32], intrinsic plasmons, and magnetoplasmons in unpatterned epitaxial graphene [33]. Being polar crystals, SiC substrates are of significant interest for SEIRA applications because they facilitate effective coupling of electromagnetic radiation to SPhPs in the epi-G layer [21, 34], which covers the frequency range $800-1000\ \mathrm{cm}^{-1}$ (in SiC, $\omega_{TO} = 796\ \mathrm{cm}^{-1}$, $\omega_{LO} = 972\ \mathrm{cm}^{-1}$ [35]). In combination with the plasmonic mechanism of light–matter interaction, they offer a prospective alternative to CVD-graphene-based technology for biosensing and chemical detection applications. In addition, the coupling effect of SPPs and SPhPs in the epi-G provides a mechanism for regulating the Casimir force and may potentially lead to its precise experimental measurement at the nanoscale [36]. However, despite the pronounced effects and good correlation with theoretical models [37, 38], the light-plasmon interaction in epi-G structures has not been well studied experimentally compared to G-on-SiO_2. The difference in the substrate dielectric constant may be expected to result in application-important divergences in the plasmonic properties of epi-G structures. Simultaneously, the higher frequency range of the TO-phonon peak and its larger refractive index in SiC compared to SiO_2 allow more distinct studies of plasmon properties in the low-frequency range, where the plasmon–plasmon interaction is not as pronounced.

In this study, we demonstrated the plasmonic response of GNR arrays fabricated using large-scale epi-G. We showed that the extinction spectra were described well by the damped oscillator model, confirming the plasmonic nature of the resonances. Unlike CVD GNRs on SiO_2, the position of the plasmon peak of epi-G GNR in the frequency range below the reststrahlen band exhibited only a weak dependence on the ribbon width. Furthermore, we performed numerical simulations using the Fourier modal method (FMM), which agreed well with the experimental spectra. These results provide new insights into the substrate-induced effects on graphene plasmons and demonstrate that epi-G enables stable substrate-coupled plasmonic excitations suitable for IR photonic applications.

Results

Samples The GNR arrays (Fig. 1a) were fabricated from epi-G and designed with grating periods ranging from 1 to 2 µm. For all samples, the ribbon width W ($W \in [500; 1000]$ nm) and inter-ribbon spacing L were equal, resulting in a fixed filling factor $r = W/(W + L) = 0.5$. The patterned area in each sample was $1\ \mathrm{mm} \times 1\ \mathrm{mm}$.

Experimental setup. We measured the Fourier transform infrared spectroscopy (FTIR) transmission spectra of the GNR arrays in a spectral window from 50 cm^{-1} to 700 cm^{-1} with a resolution of 8 cm^{-1}. The sample was mounted behind an aperture to suppress the diffraction effects so that

$$a > d \gg h,$$

where a is the array size, d the aperture diameter, and h the aperture-to-sample distance. A schematic of the experimental set-up is shown in Fig. 1b.

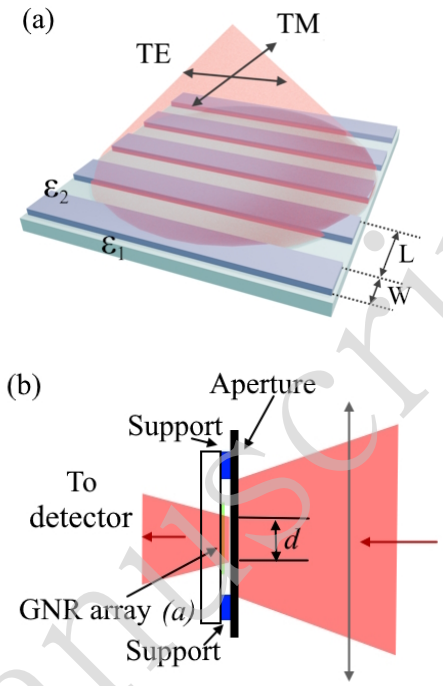

Fig. 1. (a) Schematic of the GNR array with TM and TE mode representations. The dielectric constant of epi-G is ε_2 and that of the SiC substrate is ε_1. (b) Schematic of the GNR array sample inside the FTIR spectrometer. The thickness of the supports was chosen such that diffraction effects were negligibly small.

Normally, the incident radiation is linearly polarised, with a polarisation purity exceeding 99% over the full spectral range. During the measurements, the orientation of the sample was fixed, and the polariser was rotated to record spectra in the transverse electric (TE) mode, wherein the incident electric field was parallel to the graphene ribbons, and the transverse magnetic (TM) polarisation mode, wherein the electric field was perpendicular to the ribbons (Fig. 1a). The transmission spectra of the empty aperture were recorded under the same polarisation conditions as a reference.

Raman measurements. We characterised the GNR samples using Raman microscopy. The results confirmed the

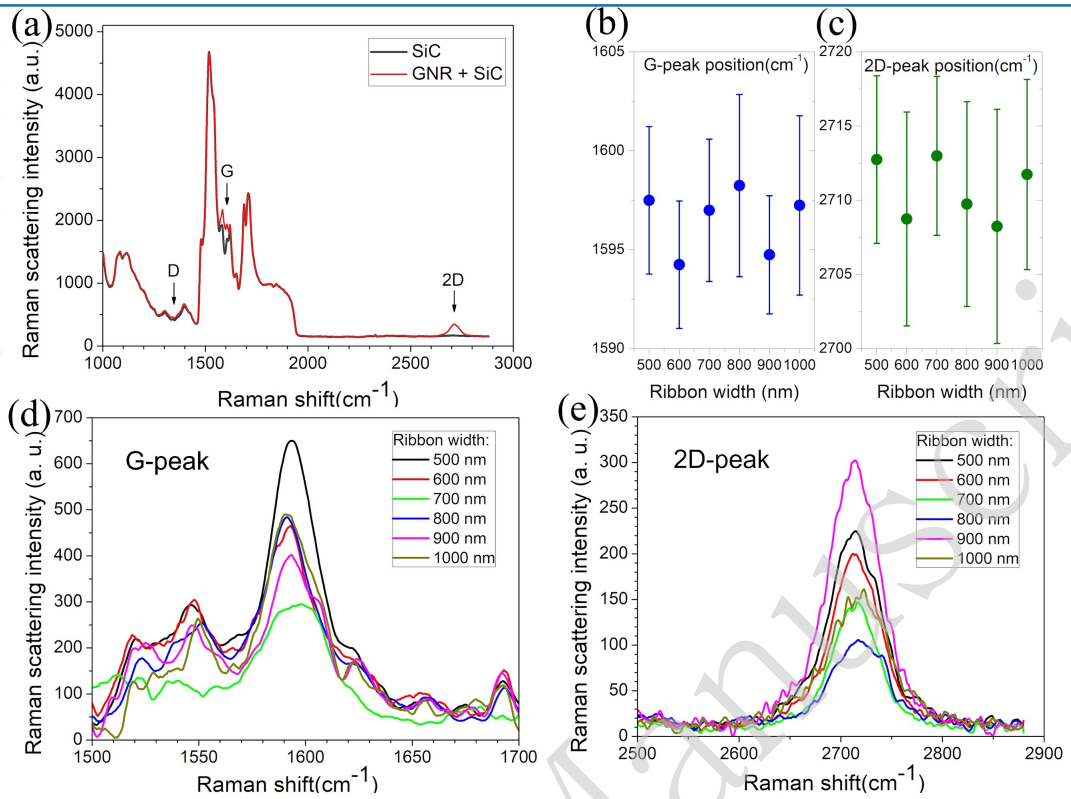

Fig. 2. Raman characterisation of samples (laser wavelength = 532 nm, laser power = 8.5–17 mW, acquisition time = 20–50 s). (a) Raman spectra of the SiC substrate (black) and a GNR on the SiC sample (red; ribbon width = 600 nm) with the poorly visible D and well-pronounced G and 2D graphene peaks. The G and D peaks are surrounded by the dominating peaks of the SiC substrate. (b), (c) Variation of the G- and 2D-peak positions from sample to sample and between various points of each GNR sample. Dots and bars are the mean and standard deviation of the peak position of a GNR sample averaged over four measurements. (d), (e) Examples of G and 2D peaks obtained as the difference between the GNR on SiC and the pure SiC Raman spectra. The G peak is surrounded by small peaks, which are the remainder of the subtracted SiC peaks.

presence of a graphene layer on top of the SiC substrate (Fig. 2). The stand-alone 2D peak was clearly visible, whereas the G peak could be extracted from the surrounding multiple SiC peaks of greater amplitude by normalising the difference between the sample and substrate spectra. This provided a good peak position but also affected its amplitude. The shape of the 2D peak depends on the number of graphene layers [39].

The spectra presented in Fig. 2e can be attributed to mono- or bilayer graphene, and considering the 2D-peak position (2710 cm^{-1}) and width (60 cm^{-1}), we assumed that the studied GNR samples consisted predominantly of monolayer graphene, since the 2D peak for bilayer graphene is typically wider (90 cm^{-1}) and located near 2740 cm^{-1} [39]. Both the G- and 2D-peak positions are strongly related to the Fermi energy of graphene [39]. We measured the Raman spectra at four different points on each sample. The average sample peak positions are shown in Fig. 2b,c, where the error bars represent the standard deviation. For both peaks, the standard deviation of the mean value (1.5 and 1.9 cm^{-1} for the G and 2D peaks, respectively) was sufficiently less than the average standard deviation of a single sample (2.5 and 3.5 times for the G and 2D peaks, respectively); i.e., the peak position variation within one sample was greater than that from sample to sample.

Since the FTIR transmission spectra were measured from the entire sample area, we studied the average GNR plasmon extinction. In this case, the plasmon peak position is defined by the mean Fermi energy, and the plasmon width arises from both plasmon scattering and the inhomogeneity of the Fermi energy over the sample. Thus, by focusing on the plasmon frequency, we can assume from the Raman spectroscopy results that the sample-to-sample inhomogeneity of the Fermi energy can be neglected. For a rough estimation of the Raman-spectra-based value, we applied the G-peak position to the Fermi energy dependence from Ref. [39] and arrived at E_F = 230±30 meV (1850±240 cm^{-1}), which agreed with the data obtained from the FTIR

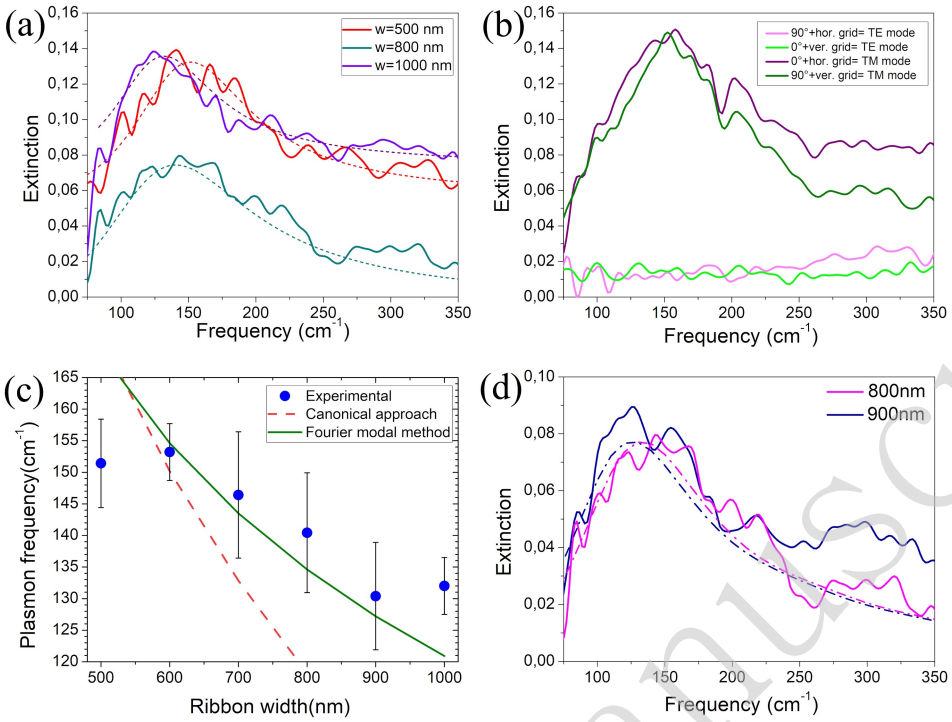

Fig. 3. (a) Plasmon extinction of GNR arrays with a ribbon width = 500 nm (red), 800 nm (green), and 1 μm (purple). Solid lines represent experimental data, and dashed lines the damped oscillator model fit (1). (b) Extinction peaks of two GNR arrays with the same ribbon width of 600 nm but various grating orientations (horizontal (light blue and blue) and vertical (rose and violet)) and polarisation angles $\alpha = 90°$ and $0°$. (c) Dependence of resonance width on GNR width calculated using the canonical approach (dashed line) and using the FMM in comparison with experimental data. (d) Calculated FMM results using $T = 300$ K, $E_F = 250$ meV (2026 cm^{-1}), $\hbar\nu = 15$ meV ($\nu = 121$ cm^{-1}) (dashed line) and experimental (solid line) extinction spectra for GNR arrays for 800 nm (magenta) and 900 nm (blue).

studies and used in the simulations included below.

FTIR experimental results. The transmission spectra of the GNR arrays, $\tau_{GNR}(\omega)$, and the pure SiC substrate, $\tau_{SiC}(\omega)$ were used to obtain the extinction, $\eta_\varepsilon(\omega)$, of the GNR arrays:

$$\eta_\varepsilon(\omega) = 1 - \frac{\tau_{GNR}(\omega)}{\tau_{SiC}(\omega)}. \quad (1)$$

The extinction spectra for the TM polarisation of the samples with ribbon widths of 500, 800, and 1000 nm are shown in Fig. 3c)). The spectra exhibited a pronounced peak near 150 cm^{-1} in the TM mode, which was due to the absorption of radiation by the surface plasmons. The peak position shifts from 130 to 153 cm^{-1} as the ribbon width decreases.

We measured two types of gratings of the same ribbon width, $W = 600$ nm, with mutually perpendicular ribbon directions (called "vertical" and "horizontal") while keeping the light polarisation fixed at 0° or at 90° to ensure that the plasmon peak originated in the breaking of the translational symmetry by the GNR grating and not due to the intrinsic spatial confinement caused by SiC step bunching in epi-G itself. Fig. 3 (b) shows the four extinction spectra of both the arrays with incident radiation in two directions. One polarisation, 0°, is set parallel to the "vertical" ribbons and perpendicular to the "horizontal" ones. Another polarisation, 90°, is, contrariwise, set perpendicular to the "vertical" grating and parallel to the "horizontal" one. The plasmon peaks of both arrays were present for the TM mode of GNR grating, as expected.

Discussion

We provide an analytical model for plasmon excitation as well as the results of the simulations using the FMM, which explicitly accounts for the substrate-induced effects on the electromagnetic field distribution, to understand in depth the experimentally observed plasmon response in GNR arrays.

Canonical models. The plasmon extinction peak can be described by a damped oscillator as follows:

$$\eta_\varepsilon(\omega) = \frac{2D_p}{\pi} \frac{\omega^2\Gamma_p}{\hbar^2(\omega^2 - \omega_p^2)^2 + \omega^2\Gamma_p^2}, \quad (2)$$

where ω is the radiation frequency, D_p the oscillator strength, $\Gamma_p = \hbar\nu$, ν the plasmon scattering rate, ω_p the plasmon frequency, and $\hbar$ the reduced Planck's constant. The Fermi energy of the GNR is calculated from the oscillator strength as [13]:

$$E_F = \frac{D_p n_{01}^2}{2\pi\alpha r}\frac{\pi\hbar\nu}{\pi\hbar\nu - D_p n_{01}}, \tag{3}$$

where α is the fine structure constant and $n_{01} = (n_0 + n_1)/2 \approx 2.1$ the average refractive index of the ambient air and SiC ($n_1 \approx 3.2$). Here, we accounted for the radiative damping of the plasmons [13].

The value derived from Maxwell's equations under the quasi-static approximation for THz plasmon resonances in graphene micro-ribbon arrays [11] yields a square-root plasmon dispersion on the ribbon width:

$$\hbar\omega_p = \sqrt{2\pi\frac{e^2 E_F}{W\kappa}}, \tag{4}$$

where E_F is the Fermi energy and $\kappa \approx 5.6$ the average dielectric constant of the surrounding media. The model used to derive Eq. (4) assumes that the plasmon scattering rate, plasmon–plasmon interactions, and plasmon radiative damping are negligible. If these effects are considered, the plasmon frequency will be red-shifted [13]:

$$\hbar\omega_p = \sqrt{2\pi\frac{e^2\Lambda(r)}{W\kappa}E_F - \hbar^2\nu^2}, \tag{5}$$

where $\Lambda(r)$ is a dimensionless parameter that reflects the effect of plasmon–plasmon interactions, which depends on the GNR filling factor and, in our case, on $\Lambda(0.5) \approx 0.653$.

For modelling the experimental plasmon dispersion law using (4) or (5), we used the scattering rate and Fermi energy obtained from the measured spectra with (1)–(3). We considered the homogeneous distribution of defects, inhomogeneities, and graphene doping levels throughout all the arrays, as all the studied GNR arrays were fabricated simultaneously on a single chip. This consideration was also confirmed by the results of the Raman studies presented above. Thus, from (2), we obtained a set of plasmon scattering rate values for each array, whose mean and standard deviation are $\nu = 110 \pm 20$ cm^{-1}. We substituted ν with (3) to obtain the Fermi energy of each array, which we averaged to obtain $E_F = 300 \pm 80$ meV (2400 ± 600 cm^{-1}). The calculated plasmon frequencies are presented in Table 1. The non-interacting model (4) overestimates the plasmon frequency. We used the lowest value of the Fermi energy within the confidence interval, $E_F = 220$ meV (1774 cm^{-1}) to get closer to the experimental values. The interacting model (5) predicted the plasmon frequency range significantly better. However, the predicted decrease in the plasmon frequency with an increase in the ribbon width significantly exceeded the experimental trend (see Table 1 and Fig. 3c).

Table 1: Plasmon frequencies for various ribbon widths. Here $\omega_{p,exp}$ are experimental data, $\omega_{p,(4)}$ are calculated from (4) using the lowest possible value of E_F within the confidence interval, $E_F = 220$ meV (1774 cm^{-1}), $\omega_{p,(4)avd}$ are calculated from (5) using the mean values $E_F = 300$ meV (2419 cm^{-1}) and $\nu = 110$ cm^{-1}, $\omega_{p,(5)exp}$ are calculated from (5) using the experimental values of E_F and ν, and $\omega_{p,FMM}$ are calculated using the FMM with $E_F = 250$ meV (2016 cm^{-1}). All frequency values are given in cm^{-1}.

W, nm	$\omega_{p,exp}$	$\omega_{p,(4)}$	$\omega_{p,(5)avd}$	$\omega_{p,(5)exp}$	$\omega_{p,FMM}$, cm^{-1}
500	151	215	172	185	169
600	153	196	150	167	155
700	146	181	133	76	144
800	140	170	118	139	135
900	130	160	105	92	127
1000	132	152	94	87	121

Fourier modal method. We performed full-wave electromagnetic simulations using the FMM [40] to describe the behaviour of the GNR arrays theoretically, without any specific approximations. The model structure in these simulations consisted of a graphene layer, which was homogeneous in the Y and Z directions and periodic in the X direction, placed between a semi-infinite air superstrate and SiC or SiO_2 substrate. The solutions to Maxwell's equations were obtained by expanding the electric and magnetic fields into Floquet–Fourier harmonics and truncating the series at 101 harmonics (see Supplemental Materials for details on the convergence of our numerical scheme).

We used the effective dielectric permittivity to incorporate the electromagnetic response of graphene into these simulations. The effective permittivity was directly derived from the surface conductivity of graphene using the following expression:

$$\varepsilon_g(\omega) = 1 + \frac{i\sigma(\omega)}{\omega\varepsilon_0 d}, \tag{6}$$

where d is an artificial thickness representing the graphene layer in the simulation, $\sigma(\omega)$ the complex surface conductivity, ε_0 the vacuum permittivity, and ω the angular frequency. The surface conductance $\sigma(\omega)$ is the sum of the contributions from the intraband and interband transitions [41]:

$$\sigma(\omega) = \sigma_{\text{intra}}(\omega) + \sigma_{\text{inter}}(\omega). \tag{7}$$

The surface conductivity determined by intraband electron–photon scattering processes can be obtained from the Drude model, which gives the following expression:

$$\sigma_{\text{intra}}(\omega) = \frac{iG_0 k_B T}{\pi\hbar(\omega + i\nu)}\ln\left(2\cosh\frac{\mu}{2k_B T}\right), \tag{8}$$

where $G_0 = 2e^2/h$ is the quantum conductance. The contribution from the inter-band transition is expressed as

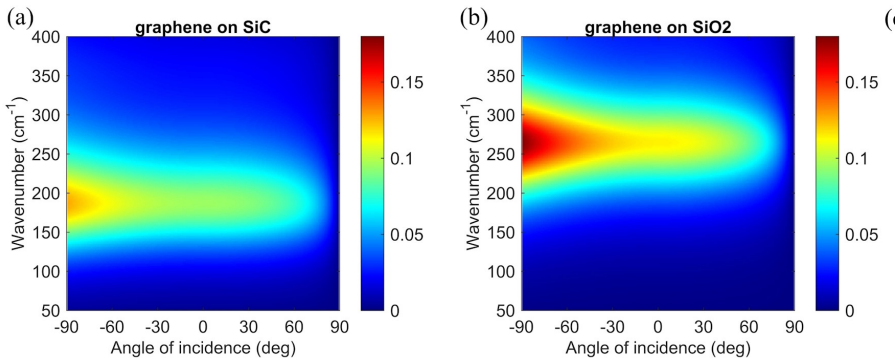

Fig. 4. Angular dependence of the extinction spectrum for graphene ribbons on the (a) SiC and (b) SiO_2 substrates calculated using the FMM using the following parameters: $E_F = 250$ meV (2026 cm^{-1}), $T = 300$ K, $\hbar\nu = 15$ meV ($\nu = 121$ cm^{-1}). (c) Schematic of the field orientation of the incident radiation with the angle of incidence being $-90°$ (top) and $+90°$ (bottom).

follows [42]:

$$\sigma_{\text{inter}}(\omega) = \frac{G_0}{8}\left[G\left(\frac{\hbar\omega}{2}\right) + i\frac{4\hbar(\omega+i\nu)}{\pi}\int_0^{+\infty}\frac{G(\epsilon)-G(\hbar\omega/2)}{\hbar^2(\omega+i\nu)^2-4\epsilon^2}d\epsilon\right],$$

where

$$G(\epsilon) = \frac{\sinh\left(\frac{\epsilon}{k_BT}\right)}{\cosh\left(\frac{\mu}{k_BT}\right)+\cosh\left(\frac{\epsilon}{k_BT}\right)}. \quad (9)$$

The dielectric response of the SiC substrate was described by the Lorentz oscillator model for a polar crystal, where the permittivity is given by:

$$\varepsilon(\omega) = \varepsilon_\infty\left(1+\frac{\omega_{LO}^2-\omega_{TO}^2}{\omega_{TO}^2-\omega^2-i\Gamma\omega}\right), \quad (10)$$

with $\varepsilon_\infty = 6.7$, longitudinal optical phonon frequency $\omega_{LO} = 972$ cm^{-1}, transverse optical phonon frequency $\omega_{TO} = 796$ cm^{-1}, and damping constant $\Gamma = 4.78$ cm^{-1}. The dielectric function of the SiO_2 substrate has been previously expressed [43].

The results of the calculations are shown in Fig. 3d. Both the spectral position and the shape of the plasmon resonance peak agreed well with the experimental data. Moreover, the plasmon dispersion calculated using the FMM better described the experimental data than the interacting model (5) (see Table 1 and Fig. 3d). This indicates that the FMM provides an effective framework for modelling plasmonic excitations in graphene structures on strongly dispersive substrates.

Figure 4 presents the angular dependence of the extinction spectrum, as calculated using the FMM, for GNR arrays on the (a) SiC and (b) SiO_2 substrates. The positive range of the incidence angle corresponded to the inclination in the $(\vec{k},\vec{E})$ plane, whereas the negative range corresponded to the inclination in the $(\vec{k},\vec{H})$ plane (Fig. 4c). In both configurations, the spectral position of the primary resonance peak exhibited a weak dependence on the angle of incidence. This behaviour is a property of a localised plasmonic mode, as its frequency is predominantly determined by the geometry, intrinsic properties of the nanostructure, and dielectric permittivity of the surroundings, rather than by the in-plane momentum provided by the incident wave, consistent with observations in systems with gold nanostripes, such as Ref. [44, 45, 46]. A notable difference between the two substrates is the overall magnitude of extinction; the peak value for the epi-G-based structure is generally lower than that for the SiO_2-based one. Furthermore, across the entire angular range, the peak extinction coefficients exhibited a gradual variation in both cases. This modulation arises from the change in coupling efficiency between the incident radiation and the plasmon mode, as the projection of the incident wavevector and the field polarisation are altered by the angle, thereby affecting the excitation conditions for the localised plasmon.

The electromagnetic field distributions calculated using the FMM for a p-polarised plane wave at normal incidence on the GNR array are presented in Fig. 5 in the (x,z) cross section at the resonant frequencies (170 cm^{-1} and 270 cm^{-1}, respectively). The first row in Fig. 5 displays the electric field energy density $|E|^2(x,z)$, revealing pronounced local maxima at the edges of the graphene ribbon. This spatial localisation is a characteristic of dipole resonance excited by the incident radiation. The resonance is further elucidated using the vector field components, E_x and E_z, as shown in the second and third rows, respectively. Their distributions exhibited a symmetric dipolar pattern centred on each ribbon. Finally, the local polarisation ellipses,

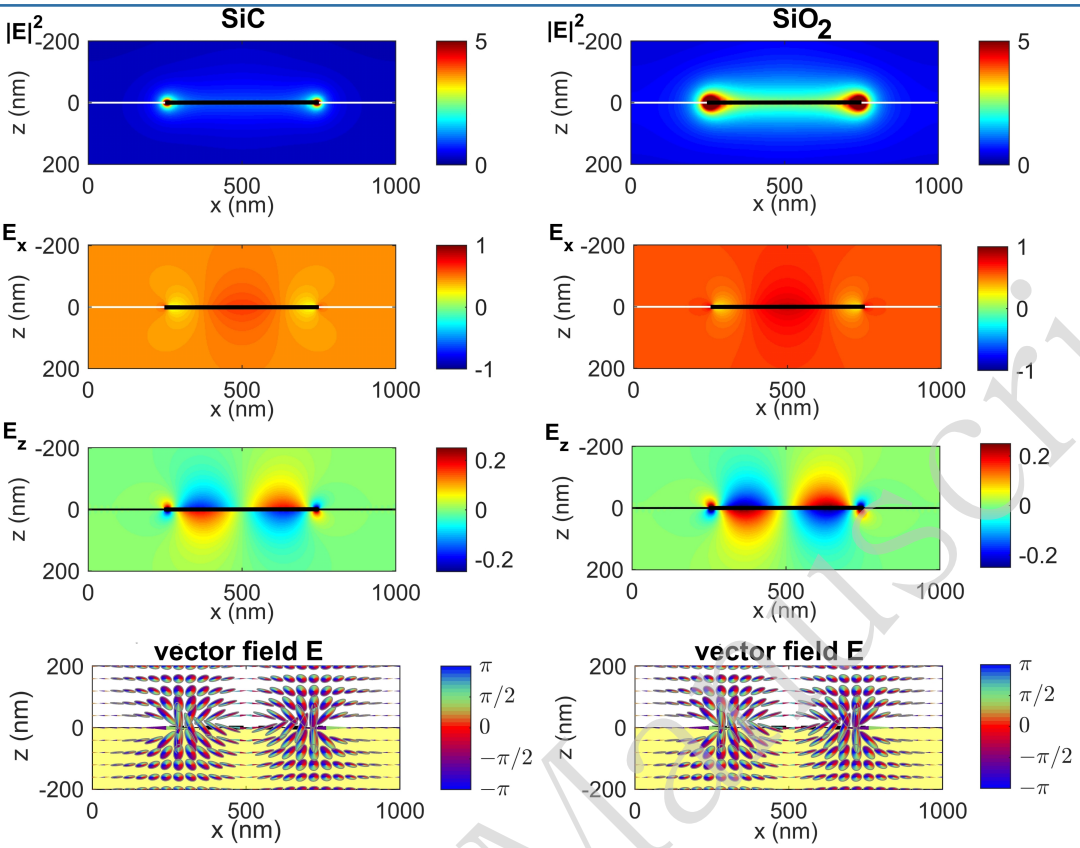

Fig. 5. Field distributions for a p-polarised plane wave normally incident on a periodic array of graphene ribbons. Left column: ribbons on a SiC substrate at 170 cm^{-1}. Right column: ribbons on a SiO_2 substrate at 270 cm^{-1}. From top to bottom: electric field energy density $|E|^2$, x-component of the electric field E_x, z-component E_z, and local polarisation ellipses, colour-coded by the instantaneous phase of the electric field. The field patterns confirmed the excitation of a dipole plasmon resonance localised at the ribbon edges. Calculations were made using the FMM for $T = 300$ K, $E_F = 250$ meV (2026 cm^{-1}), and $\hbar\nu = 15$ meV ($\nu = 121$ cm^{-1}).

colour-coded according to the instantaneous phase of the electric field, are shown in the last row. Despite the different substrate permittivities (for SiC and SiO_2) and corresponding resonant frequencies, the field morphologies in both cases were remarkably similar, indicating that the fundamental plasmonic resonance is primarily dictated by the geometry and properties of the graphene itself, with the substrate acting mainly to scale the resonant frequency.

This mode consisted of two hot spots localised at the ribbon edges. The strength of the interaction between the two hot-spots within the same ribbon determines the extent to which the resonance frequency depends on the ribbon width. As indicated by the field distributions shown in Fig.5, the field decays more rapidly away from the ribbon for a higher-index substrate (a common situation for edge or surface waves). This stronger confinement reduces the overlap between the two edge hot spots, leading to a weaker dependence of the peak position on the ribbon width.

Conclusion

We demonstrated that GNR arrays on SiC exhibit polarisation-sensitive plasmon resonances with a weak period dependence, by contrast to CVD graphene on SiO_2 substrates. Thus, the GNR composed of epi-G provided a robust platform for plasmonic devices requiring high spectral stability. The theoretical model of the GNR in epi-G supports our experimental observations.

The extinction spectra calculated using the FMM accurately reproduced the spectral position and the line shape of the plasmon resonance. These results demonstrate that the FMM provides a reliable theoretical framework for describing plasmonic excitations in graphene structures on strongly dispersive substrates. The findings highlighted the crucial role of the substrate in determining the plasmonic properties of graphene nanostructures and provided new perspectives for designing of tuneable plasmonic and photonic devices based on epitaxial graphene on SiC.

Materials and methods

Sample fabrication. The fabrication of GNR arrays from epi-G involved the following steps: first, the GNR pattern was defined in a photoresist mask using optical lithography. The pattern was subsequently transferred onto the graphene layer via oxygen plasma etching. After etching, the remaining resist was removed by dissolving in acetone, leaving only the GNR array on the SiC substrate. The GNR chip design is composed of a 5×5 matrix of arrays oriented in two mutually perpendicular directions. The size of each array was 1×1 mm^2, and the spacing between neighbouring patterns was 0.7 mm. A 0.05 mm thick support step was fabricated along the edge of the chip around the matrix of GNR patterns.

FTIR measurements. We performed spectral measurements using an FTIR spectrometer (Bruker IFS 125HR) in the radiation transmission mode with a resolution of 8 cm^{-1}. The sample chip was mounted on a diaphragm with a hole diameter of 0.5 mm facing the incident radiation, and the distance to the surface of the diaphragm was 0.05 mm; thus, the light passed entirely through the GNR array being measured. We used a helium-cooled Si bolometer as a detector to achieve the required plasmon fitting signal-to-noise ratio in the spectral window of interest (50 cm^{-1} to 700 cm^{-1}). We mounted a metal-grid linear polariser with a polarisation purity exceeding 99% over the full spectral range in front of the diaphragm, which allowed setting the polarisation direction arbitrarily.

Acknowledgement

We acknowledge support from the Russian Science Foundation (Project No. 25-79-31023). This research was partly conducted using the research equipment of the shared facility centre at the PN Lebedev Physical Institute of RAS.

Author contributions

The experiments were conceived by V. N. A. Sample fabrication and preparation by S. R. Y. Experimental FTIR investigations and analysis of the results were performed by O. A. K., A. A. K., and A. V. M. Raman spectra measurements were performed by D. M. Z. Theoretical modelling and calculation of optical properties via the Fourier modal method (FMM) were conducted by S. A. D. using an approach proposed by N. A. G. The manuscript was drafted by O.K. and A.K., with significant input from S.D. on the theoretical sections.

Data Availability

All data are available from the corresponding authors upon request.

Conflict of interest

The authors declare no conflicts of interest.

References

[1] Low, T. & Avouris, P. Graphene plasmonics for terahertz to mid-infrared applications. *ACS Nano* **8**, 1086–1101 (2014).

[2] Basov, D. N., Fogler, M. M. & García de Abajo, F. J. Polaritons in van der waals materials. *Science* **354**, eaag1992 (2016).

[3] Caldwell, J. D. et al. Photonics with hexagonal boron nitride. *Nature Reviews Materials* **4**, 552–567 (2019).

[4] Kennes, D. M. et al. Moiré heterostructures as a condensed-matter quantum simulator. *Nature Physics* **17**, 155–163 (2021).

[5] Zhang, Q. et al. Interface nano-optics with van der waals polaritons. *Nature* **597**, 187–195 (2021).

[6] Dai, S. et al. Tunable phonon polaritons in atomically thin van der waals crystals of boron nitride. *Science* **343**, 1125–1129 (2014).

[7] Caldwell, J. D. & Novoselov, K. S. Mid-infrared nanophotonics. *Nature Materials* **14**, 364–366 (2015).

[8] Brar, V. W. et al. Highly confined tunable mid-infrared plasmonics in graphene nanoresonators. *Nano Letters* **13**, 2541–2547 (2013).

[9] Langer, J. et al. Present and future of surface-enhanced raman scattering. *ACS Nano* **14**, 28–117 (2020).

[10] Mamiyev, Z. et al. Enhanced light–matter interactions with a single sn nanoantenna on epitaxial graphene. *Advanced Optical Materials* **13**, e00979 (2025).

[11] Ju, L. et al. Graphene plasmonics for tunable terahertz metamaterials. *Nature Nanotechnology* **6**, 630–634 (2011).

[12] Autore, M. et al. Boron nitride nanoresonators for phonon-enhanced molecular vibrational spectroscopy at the strong coupling limit. *Light: Science Applications* **7**, 17172 (2017).

[13] Semenenko, V. et al. Plasmon–plasmon interactions and radiative damping of graphene plasmons. *ACS Photonics* **5**, 3459–3465 (2018).

[14] Klimenko, O. et al. Tunable graphene plasmons in nanoribbon arrays: the role of interactions. *Optical Materials Express* **11**, 1390–1400 (2021).

[15] Yang, X. X. et al. Nanomaterial-based plasmon-enhanced infrared spectroscopy. *Advanced Materials* **30**, 1704896 (2018).

[16] Rodrigo, D. et al. Mid-infrared plasmonic biosensing with graphene. *Science* **349**, 165–168 (2015).

[17] Hu, H. et al. Far-field nanoscale infrared spectroscopy of vibrational fingerprints of molecules with graphene plasmons. *Nature Communications* **7**, 12334 (2016).

[18] Khaliji, K. et al. Plasmonic gas sensing with graphene nanoribbons. *Physical Review Applied* **13**, 011002 (2020).

[19] Hu, H. et al. Far-field nanoscale infrared spectroscopy of vibrational fingerprints of molecules with graphene plasmons. *Nature Communications* **10**, 1131 (2019).

[20] Anderson, M. S. Surface enhanced infrared absorption by coupling phonon and plasma resonance. *Applied Physics Letters* **87**, 144102 (2005).

[21] Caldwell, J. D. et al. Low-loss, infrared and terahertz nanophotonics using surface phonon polaritons. *Nanophotonics* **4**, 44–68 (2014).

[22] Sarker, D. et al. Terahertz polarizer based on tunable surface plasmon in graphene nanoribbon. *Optics Express* **29**, 42713–42725 (2021).

[23] Anjali, Varshney, R. K. & Kumar, S. Actively tunable graphene ribbon based multi-band thz polarizer with a high extinction ratio. *Journal of the Optical Society of America B* **40**, 1688–1695 (2023).

[24] Lou, S. et al. Graphene nanoribbons: current status, challenges and opportunities. *Quantum Frontiers* **3** (2024).

[25] Prasad, M. D., Sharma, A. & Tambe, P. Graphene nanoribbons reinforced polymer nanocomposites and its applications: A review. *Journal of Physics: Conference Series* **2225**, 012004 (2022).

[26] Sharma, H. Graphene nanoribbon for future vlsi applications: a review. In integrated Devices for Artificial Intelligence and VLSI (eds Raj, B. et al.) (Hoboken:John Wiley & Sons, Inc., 2024), 101–123. doi:10.1002/9781394205158.ch5.

[27] Chen, J. N. et al. Optical nano-imaging of gate-tunable graphene plasmons. *Nature* **487**, 77–81 (2012).

[28] Eless, V. et al. Phase coherence and energy relaxation in epitaxial graphene under microwave radiation. *Applied Physics Letters* **103**, 093103 (2013).

[29] Yegiyan, S. R., Klimenko, O. A. & Antonov, V. N. Detection of terahertz radiation with the p-n graphene grid. *Journal of Experimental and Theoretical Physics* **168**, 208–214 (2025).

[30] Celis, A. et al. Graphene nanoribbons: fabrication, properties and devices. *Journal of Physics D: Applied Physics* **49**, 143001 (2016).

[31] Palacio, I. et al. Atomic structure of epitaxial graphene sidewall nanoribbons: Flat graphene, miniribbons, and the confinement gap. *Nano Letters* **15**, 182–189 (2014).

[32] Sorger, C. et al. Terahertz response of patterned epitaxial graphene. *New Journal of Physics* **17**, 053045 (2015).

[33] Crassee, I. et al. Intrinsic terahertz plasmons and magnetoplasmons in large scale monolayer graphene. *Nano Letters* **12**, 2470–2474 (2012).

[34] Wang, T. et al. Phonon-polaritonic bowtie nanoantennas: Controlling infrared thermal radiation at the nanoscale. *ACS Photonics* **4**, 1753–1760 (2017).

[35] Li, K. et al. Graphene plasmon cavities made with silicon carbide. *ACS Omega* **2**, 3640–3646 (2017).

[36] Hu, X. H. et al. Modulation of the casimir force via graphene plasmons-sic surface phonon polaritons coupling. *Journal of Applied Physics* **138**, 213103 (2025).

[37] Jadidi, M. M. et al. Optical control of plasmonic hot carriers in graphene. *ACS Photonics* **6**, 302–307 (2019).

[38] Rufangura, P. et al. Towards low- loss on-chip nanophotonics with coupled graphene and silicon carbide: a review. *Journal of Physics: Materials* **3**, 032005 (2020).

[39] Ni, Z. H. et al. Raman spectroscopy of epitaxial graphene on a sic substrate. *Physical Review B* **77**, 115416 (2008).

[40] Tikhodeev, S. G. et al. Quasiguided modes and optical properties of photonic crystal slabs. *Physical Review B* **66**, 045102 (2002).

[41] Falkovsky, L. & Pershoguba, S. Optical far-infrared properties of a graphene monolayer and multilayer. *Physical Review B* **76**, 153410 (2007).

[42] Hanson, G. W. Dyadic green's functions and guided surface waves for a surface conductivity model of graphene. *Journal of Applied Physics* **103**, 064302 (2008).

[43] Palik, E. D. Handbook of optical constants of solids. Volume III. (San Diego: Academic Press, 1998).

[44] Christ, A. et al. Optical properties of planar metallic photonic crystal structures: Experiment and theory. *Physical Review B* **70**, 125113 (2004).

[45] Dyakov, S. et al. Plasmon induced modification of silicon nanocrystals photoluminescence in presence of gold nanostripes. *Scientific reports* **8**, 4911 (2018).

[46] Dyakov, S. et al. Optical properties of silicon nanocrystals covered by periodic array of gold nanowires. *Physical Review B* **93**, 205413 (2016).

[47] Padmanabhan, P. et al. A graphene-based magnetoplasmonic metasurface for actively tunable transmission and polarization rotation at terahertz frequencies. *Applied Physics Letters* **116**, 221107 (2020).

[48] Jadidi, M. M. et al. Tunable terahertz hybrid metal–graphene plasmons. *Nano Letters* **15**, 7099–7104 (2015).

[49] Poumirol, J. M. et al. Magnetoplasmons in quasineutral epitaxial graphene nanoribbons. *Physical Review Letters* **110**, 246803 (2013).

[50] Das, A. et al. Monitoring dopants by raman scattering in an electrochemically top-gated graphene transistor. *Nature Nanotechnology* **3**, 210–215 (2008).